

Article

Morphology of Inclusions and Its Refinement Mechanism in the New P91 Heat-Resistant Pipeline Steel

Xiaohua Chen ^{1,*}, Shenghui Liang ², Yanlin Wang ², Zidong Wang ^{1,2,*}, Weijie Fan ¹, Xinning Yu ¹ and Jian Yang ²¹ State Key Laboratory for Advanced Metals and Materials, University of Science and Technology Beijing, Beijing 100083, China² School of Materials Science and Engineering, University of Science and Technology Beijing, Beijing 100083, China

* Correspondence: chenxh@skl.ustb.edu.cn (X.C.); wangzd@mater.ustb.edu.cn (Z.W.); Tel.: +86-10-82375388 (X.C.)

Abstract: A new type of P91 heat-resistant pipeline steel ingot was prepared by feeding Al twisted wire into a steel melt through a multi-point regional micro-supply method, combined with electro-magnetic stirring. The type, shape, and size of inclusions in the new P91 steel after forging were then analyzed by scanning electron microscope (SEM), energy dispersive spectroscopy (EDS), and transmission electron microscope (TEM). The results showed that four types of inclusions were detected in the P91 steel, including: spherical independent Al₂O₃ inclusions, irregular Al₂O₃-SiO₂ composite inclusions, nearly spherical MgO-Al₂O₃ composite inclusions, and spherical (Ca, Mg, Al) (O) composite inclusions. Compared with traditional P91 steel, the inclusions in the new P91 steel were significantly refined. Refining mechanisms of inclusion showed that Al₂O₃ oxide particles distributed dispersedly with fine sizes could be obtained through a multi-point regional micro-supply method. Further, Al₂O₃ particles act as the nucleation core to form a “core-shell” structure and play the role of a heterogeneous nucleation to refine SiO₂, MgO, (Ca, Mg) (O), and other inclusions in the steel.



Citation: Chen, X.; Liang, S.; Wang, Y.; Wang, Z.; Fan, W.; Yu, X.; Yang, J. Morphology of Inclusions and Its Refinement Mechanism in the New P91 Heat-Resistant Pipeline Steel. *Metals* **2022**, *12*, 1556. <https://doi.org/10.3390/met12101556>

Academic Editor: Christine Borchers

Received: 18 August 2022

Accepted: 14 September 2022

Published: 20 September 2022

Publisher's Note: MDPI stays neutral with regard to jurisdictional claims in published maps and institutional affiliations.



Copyright: © 2022 by the authors. Licensee MDPI, Basel, Switzerland. This article is an open access article distributed under the terms and conditions of the Creative Commons Attribution (CC BY) license (<https://creativecommons.org/licenses/by/4.0/>).

Keywords: P91 steel; regional micro-supply; inclusion refinement; heterogeneous nucleation; microstructure

1. Introduction

High temperature, high pressure pipe material is one of the most important materials found in thermal power plants; it not only plays an important role in the safety of the power plant operation, but also affects the construction investment of the power plant [1,2]. The P22 heat-resistant pipe steel used in early stages is a low-alloy heat-resistant steel with Cr and Mo as the main elements and structure of perlite, and its composition is the same as 12Cr1MoV Steel in China. Although it has good processing and welding properties, the working condition of this kind steel is harsh due to the low strength and poor heat resistance. In the follow-up project construction, 10CrMo910 steel was first used in the main steam pipeline of ultra-high pressure 125 MW and 200 MW units, but this pearlitic heat-resistant steel cannot meet the service conditions under high temperatures of 600–650 °C. Meanwhile, martensitic heat-resistant steel can be used at higher temperatures and high strength, and the typical representative is 9Cr-1Mo steel. P91 steel is a new type of steel by adding V, Nb, N, and other strengthening elements to the original 9Cr-1Mo steel [3]. P91 steel is a typical martensitic heat-resistant steel, and its maximum service temperature can reach 650 °C, which fills the vacancy of pipeline steel under high temperature conditions. The supercritical and ultra-supercritical units developed in recent years regarded P91 steel as an important steel for the mainstream pipe: the hot section of reheated main steam pipe and its corresponding high-temperature header [4–7].

The inclusion of P91 steel is an important factor affecting its properties. Its internal inclusions mainly exist in the form of non-metallic compounds, such as oxides, sulfides, nitrides, etc. Non-metallic inclusions are often the cause of surface and internal defects of steel, especially coarse inclusions, which not only worsen the cold and hot workability, but also have a negative impact on the mechanical properties, especially the fatigue properties of steel [8–11]. Due to the difference of thermal expansion coefficients between the inclusion and matrix, radial tensile force would be generated in the steel matrix around the inclusion. This stress, together with the external cyclic stress, promotes the formation of fatigue cracks in the steel matrix close to the inclusion, and worsens the fatigue performance of the steel [12]. However, inclusions with a small size and spherical contour have little deteriorated effect on steel properties [13–15]. In 1991, Murakami et al. [16] proposed the concept of the “critical size” of inclusions affecting the fatigue performance of steel. If the inclusion size was smaller than the “critical size”, it would not have a deteriorated effect on the fatigue life of steel. Sun et al. [17] found that when the inclusion size was doubled, the fatigue life of the material decreased by two orders of magnitude. Therefore, the inclusion size had a significant impact on the mechanical properties of steel. The influence of non-metallic inclusions on the fatigue properties of steel was also related to the shape of inclusions. The smaller the radius of curvature of inclusions (the sharper the contour), the more serious the stress concentrated in the steel matrix. Under the alternating stress, fatigue cracks first initiated at the sharp corners of inclusions perpendicular to the direction of tensile stress, and the crack growth rate was much faster than that of spherical inclusions. Therefore, the inclusion with the irregular shape and multiple edges and corners was more harmful to the fatigue performance than the spherical inclusion [18–20]. The refinement and spheroidization of inclusions in P91 martensitic heat resistant steel could effectively improve its properties.

In general, the inclusion grade of P91 steel is required to be below grade 2.5 (including A, B, C, D, and DS) [21]. Traditional ideas for removing inclusions mainly include gas stirring to improve molten steel flow, setting flow control devices in tundish to obtain reasonable flow field, and using filters to forcibly separate inclusions in tundish [22,23]. In this paper, a new method for optimizing the inclusion morphology in P91 steel is proposed, and the inclusion refinement mechanism is discussed. The results showed that multi-point regional micro-supply of Al elements was achieved by feeding twisted Al wire into the melt during the smelting process of P91 steel, and Al_2O_3 oxide particles are obtained with fine size and dispersive distribution. Al_2O_3 oxide particles playing the role of heterogeneous nucleation and refined SiO_2 , MgO , $(\text{Ca}, \text{Mg})\text{O}$, and other inclusions in steel. This study provided a new idea for the optimization of inclusions in steel.

2. Materials and Methods

In this paper, a new P91 steel was prepared through a multi-point regional micro-supply method combined with electromagnetic stirring technology. The chemical composition of experimental P91 steel is shown in Table 1. Schematic diagram of twisted Al wire is shown in Figure 1. Al wire with diameters of 2 mm were used for preparing the twisted wire with diameter of 9 mm.

Table 1. Chemical composition of experimental P91 steel (wt.%).

| C | Si | Cr | Mo | Mn | S | P | Nb | Ni | V | Al | Ti | Fe |
|-----|------|------|------|------|-------|------|------|------|-----|-------|-------|---------|
| 0.1 | 0.37 | 8.68 | 0.92 | 0.43 | 0.001 | 0.01 | 0.08 | 0.16 | 0.2 | 0.011 | 0.002 | balance |

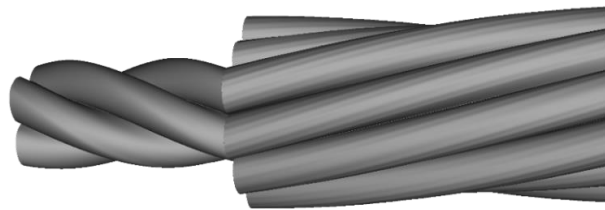


Figure 1. Schematic diagram of twisted Al wire.

The experimental process for the new P91 is as follows: electric arc furnace smelting → ladle furnace (LF) refining → multi-point regional micro-supply → vacuum degassing (VD) treatment → Nitrogen adjustment → soft blowing → mold casting → forging. Raw materials (10 tons) were selected according to the preset chemical composition (Table 1) for electric arc furnace smelting. Next, LF refining was carried out, and the free oxygen concentration was controlled at 30–100 ppm. The melt was heated to 1630 °C, and then the twisted Al wire (1.1 kg) with a diameter of 9 mm, was fed into the melt through the wire feeder with a feeding speed of 3–4 m/s. After feeding the wire, the free oxygen concentration was controlled at 10 ppm, then the VD treatment was carried out. Finally, the molten steel was poured into the mold and an ingot (diameter 1000 mm × length 2000 mm) was cast, followed by forging. The traditional process is almost the same as the new process, except that it does not have the procedure of feeding the Al wire.

Al dispersion is more uniform by adding fine Al wire combined with the effect of flow field, which is conducive to controlling the regional concentration gradient caused by the contact between alloy elements and oxygen in molten steel. The relevant implementation methods have been patented.

To improve the microstructure and mechanical properties of P91 steel, the ingot was forged after the riser was cut off. The initial forging temperature was 1000 °C, and the final forging temperature range was 800–850 °C. The initial furnace loading temperature of the steel was set at 600 °C and then rose to 850 °C, holding for 1 h. After that, the temperature rose rapidly to 1000 °C and held for one hour. Next, forging began and the temperature should have been controlled within the final forging temperature range during the forging process.

The samples were mechanically ground and polished. The inclusions in experimental P91 forged steel billets were detected according to the standard for the determination of the content of non-metallic inclusions in steel (GB/T 10561-2005).

The inclusions in samples were observed by Zeiss-Auriga SEM (Carl Zeiss AG, Oberkochen, Germany), and EDS (Oxford Instruments, High Wycombe, UK) analysis was performed to obtain the chemical composition. TEM samples cut from the steel were mechanically thinned to 35 µm thickness. Disks of 3 mm in diameter were punched from the foils and then electropolished by a twin-jet apparatus with a solution of 10 vol% HClO₄ at −20 °C to further thin them to a thickness of less than 100 nm. TEM was conducted with an FEI Tecnai F30 (FEI Company, Hillsboro, OR, USA) operated at a voltage of 300 kV.

3. Results

As shown in Figure 2, in all samples the sum of inclusion grades less than grade 1 in P91 steel prepared by traditional smelting method was less than 15% [24], while the sum of inclusion grades of experimental P91 steel obtained by multi-point regional micro-supply alloying method could all be controlled at or below grade 1.

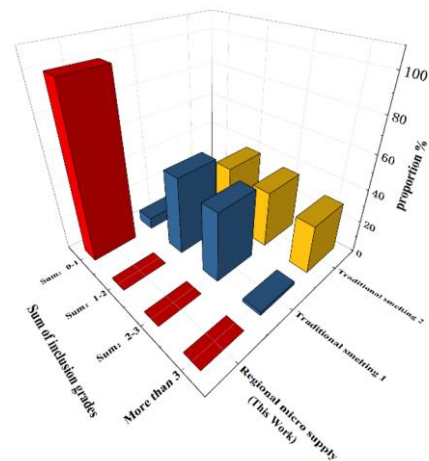


Figure 2. The proportion of sum of inclusion grades in P91 steel prepared by different methods [24].

The high-grade DS inclusions in experimental P91 steel were characterized. In general, there are four types of inclusions.

Firstly, as shown in Figure 3, Al_2O_3 inclusions are angular and spherical, which are independently distributed in the steel matrix, and their sizes are $6.8 \mu\text{m}$ and $7.7 \mu\text{m}$, respectively (Figure 3a). EDS results showed that Al_2O_3 inclusion was composed of Al, O, and Fe elements (Figure 3b–d), in which the presence of Fe was mainly caused by interference of the matrix.

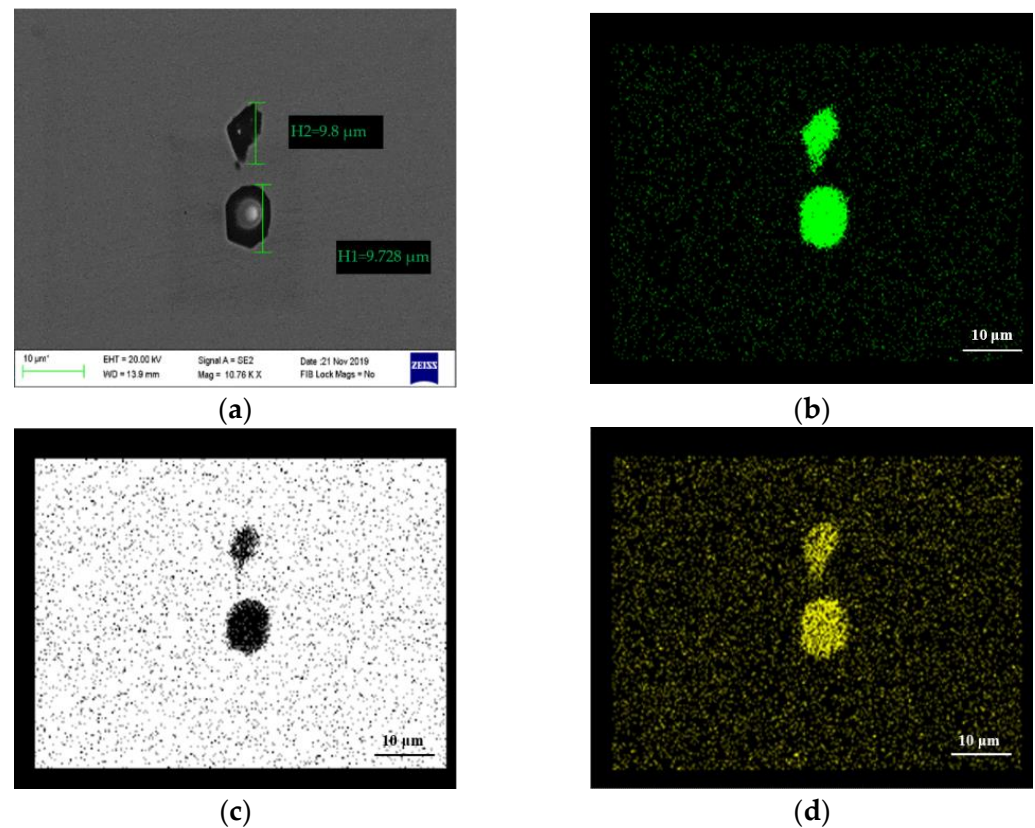


Figure 3. EDS mapping of typical Al_2O_3 inclusion in experimental P91 steel; (a) SEM image; (b) Al; (c) O; (d) Fe.

Secondly, there are $\text{Al}_2\text{O}_3\text{-SiO}_2$ composite inclusions in new experimental P91 steel. As shown in Figure 4, these DS inclusions contained Al, O, and Si elements, with a size of about 10 μm . SiO_2 in traditional P91 steel was mostly sharp single-phase inclusions with edges and corners. When being stressed, the tip of such inclusions could easily produce stress concentrations, which resulted in microcracks and became the source of cracking failure. Meanwhile, the $\text{Al}_2\text{O}_3\text{-SiO}_2$ composite inclusions in experimental P91 steel samples prepared by multi-point regional micro-supply method had a spherical shape, which was conducive to maintaining the material properties.

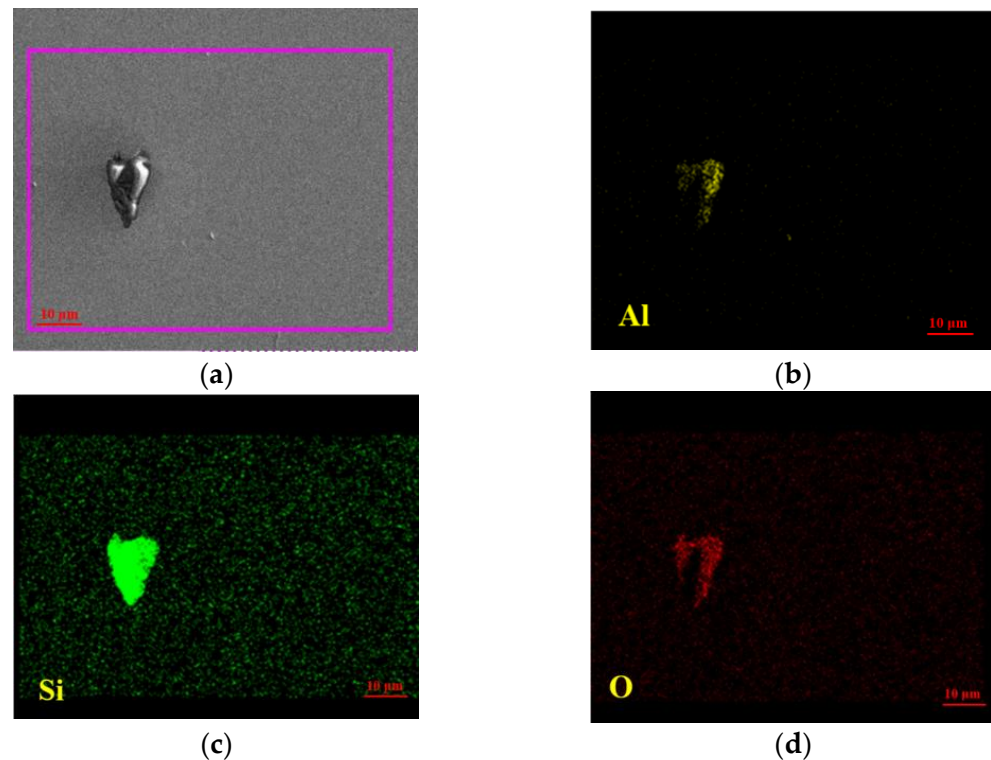


Figure 4. EDS mapping of a typical $\text{Al}_2\text{O}_3\text{-SiO}_2$ inclusion in experimental P91 steel; (a) SEM image; (b) Al; (c) Si; (d) O.

Thirdly, there are few $\text{MgO-Al}_2\text{O}_3$ composite inclusions, with a small size and a circular shape. Figure 5 showed the results of EDS mapping of one inclusion. The size of the inclusion was 10 μm , the shape was approximately spherical, and the main components were C, Al, Mg, and O. According to the point scan in Figure 5e, the contents of Al, Mg, and O elements were 42.85 wt.%, 3.48 wt.%, and 45.10 wt.%, respectively. The remaining elements were C, Fe, Cr, and other elements.

Fourthly, there are also (Ca, Mg, Al) (O) compound inclusions in experimental P91 steel. The structure was nearly spherical and the size was about 5–27 μm . As shown in Figure 6, the matrix of the whole inclusion was Al_2O_3 . The size of inclusion was 26.60 μm . It can be seen that most of the spherical inclusion was composed of Al_2O_3 , and the elements from the outside to the inside were S, Ca, and Mg, respectively. Sulfide was attached to the periphery of the compound inclusion, forming a “core-shell” structure. The inclusion “core” was mainly the composite oxide inclusion formed by CaO, MgO, and Al_2O_3 , et al.

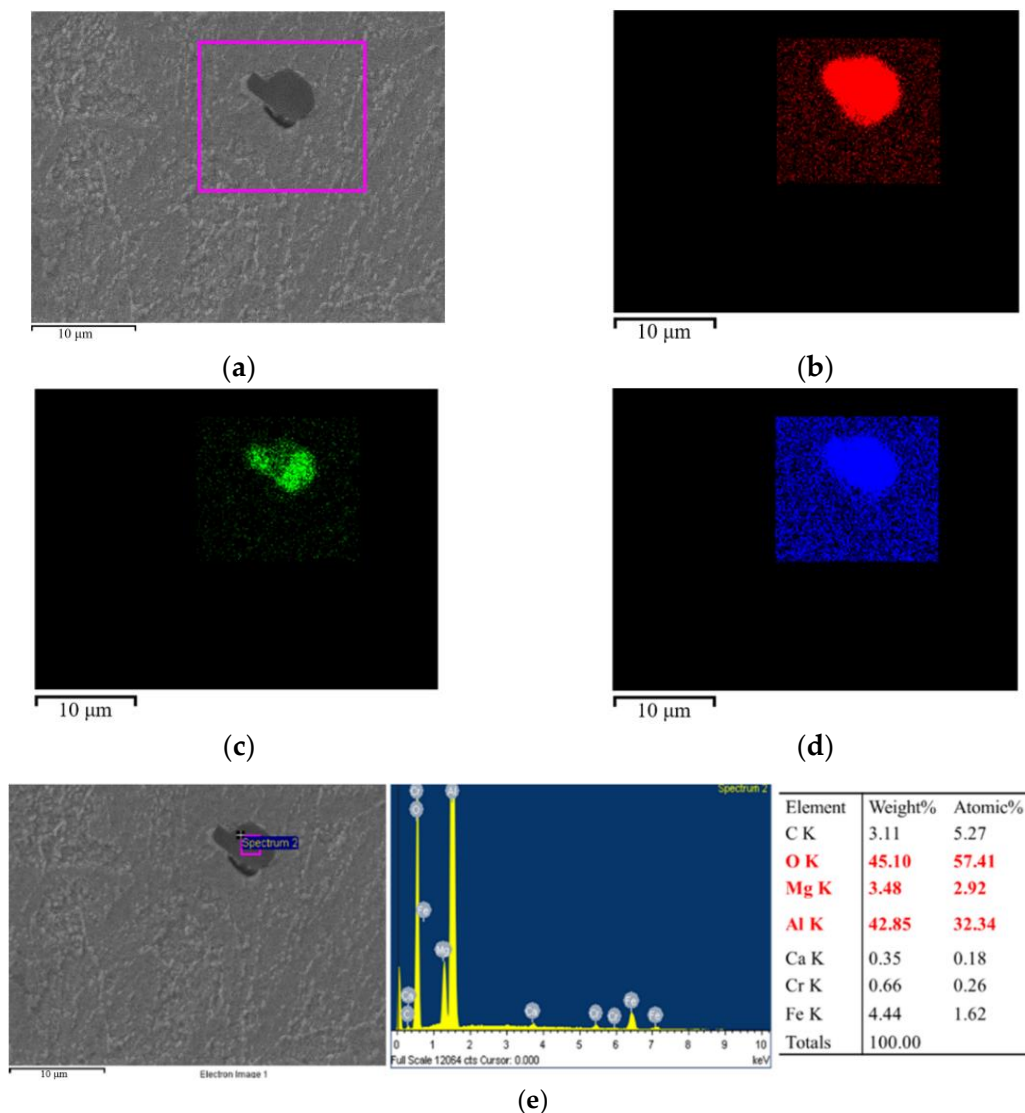


Figure 5. EDS results of typical Al_2O_3 -MgO complex inclusion in experimental P91 steel; (a) SEM image; (b) Al mapping; (c) Mg mapping; (d) O mapping; (e) Results of EDS point scanning.

Figure 7 showed the EDS mapping for Al_2O_3 inclusion at micron scale. Inclusion was analyzed by TEM, as shown in Figure 8a,b. According to the analysis of TEM and diffraction pattern calibration, the central part was Al_2O_3 , which was surrounded with Cr_7C_3 . Al_2O_3 was uniformly and densely distributed, and carbides grew on the periphery of Al_2O_3 . It was found that the micron-magnitude precipitates were precipitated by adopting nano Al_2O_3 oxide as nucleation particle. Therefore, it could be deduced that nano alumina particles might exist as the nucleation core during the formation of a shell structure.

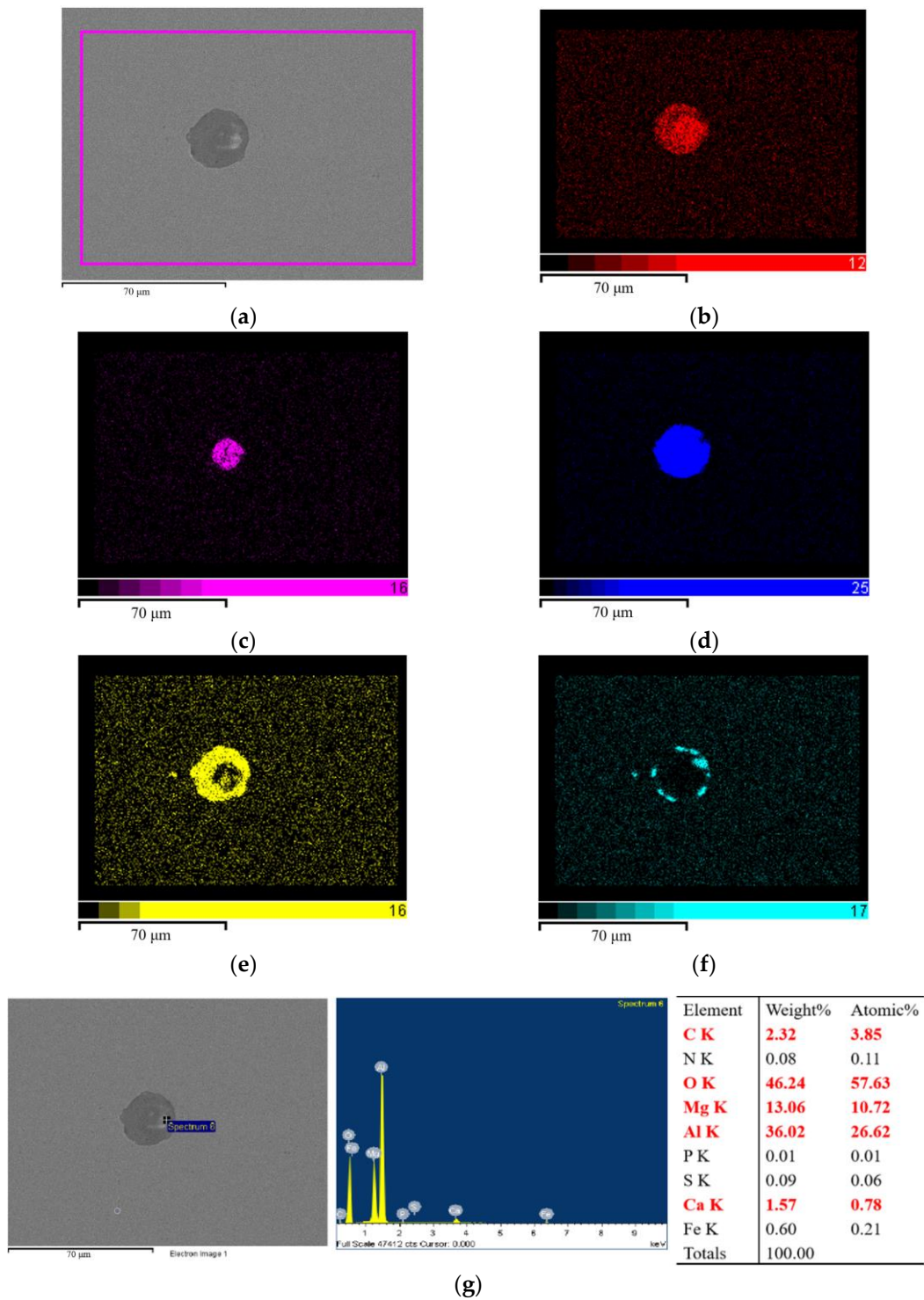


Figure 6. EDS results of typical $\text{Al}_2\text{O}_3\text{-MgO}$ complex inclusion in experimental P91 steel; (a) SEM image; (b) O; (c) Mg mapping; (d) Al mapping; (e) Ca mapping; (f) S mapping; (g) Results of the EDS point scanning.

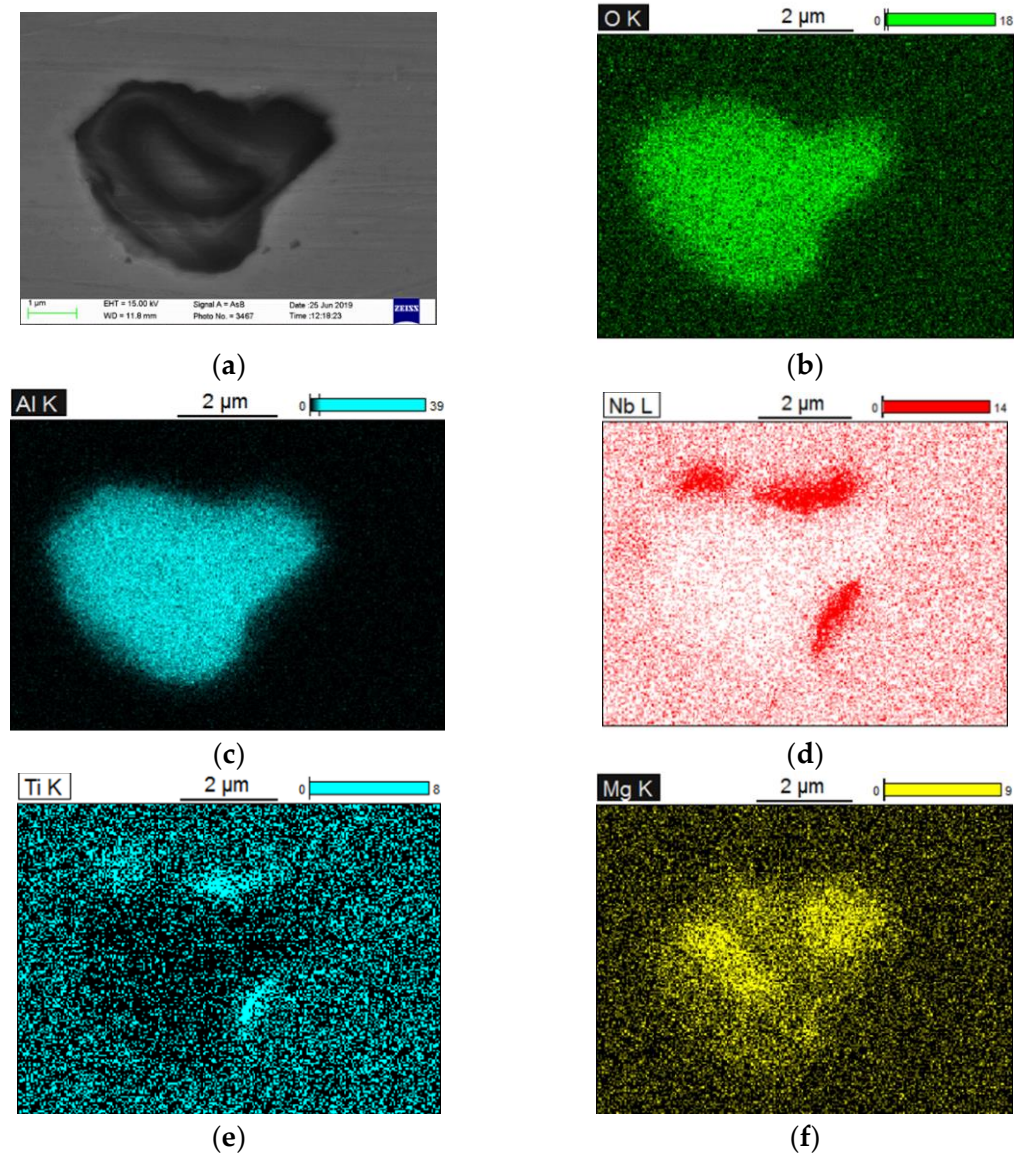


Figure 7. EDS mapping of Al_2O_3 at micron scale; (a) SEM image; (b) O; (c) Al; (d) Nb; (e) Ti; (f) Mg.

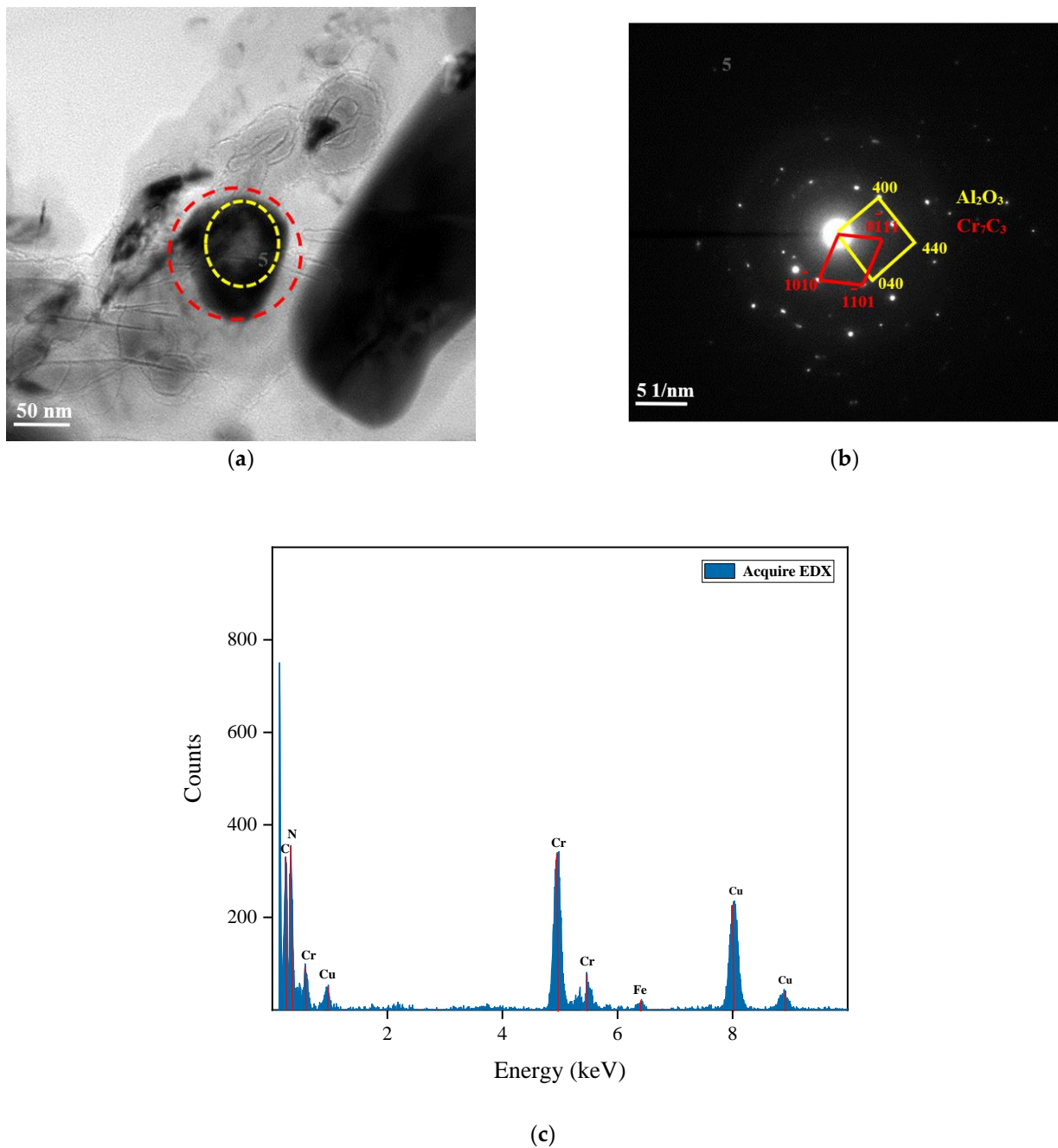


Figure 8. (a) TEM image of inclusion; (b) Diffraction pattern of inclusion; (c) EDS results of inclusion; Number 5 represents the fifth point for EDS scanning; The outer region surrounded by yellow line is Cr_7C_3 , and inner region surrounded by red line is Al_2O_3 .

4. Discussion

The thermodynamic and dynamics conditions of oxide growth in molten steel were discussed. Based on the thermodynamic analysis of oxide nucleation and growth in steel, the nucleation size, nucleation rate, and inclusion nano-crystallization process of alumina in high-strength steel were analyzed qualitatively and quantitatively. The following Equation (1) [25] was used to calculate the critical nucleation radius of oxide particles in melts.

The critical nucleation radius:

$$R^* = \frac{2\sigma T_m}{L_m \Delta T} \quad (1)$$

where σ is specific surface energy; T_m is theoretical melting point of Al_2O_3 ; L_m is the melting heat of Al_2O_3 ; ΔT is the difference between T_m (2051 °C) [26] and actual solidification temperature. The parameters in the above equations are as follows: $\sigma = 2.6 \text{ J/m}^2$ [27], $L_m = 94.14 \text{ kJ/mol}$ [28].

When the aluminum wire was fed into the molten steel, it reacted with the oxygen in the molten steel. The critical nucleation radius was related to the temperature of the molten steel, which was generally 1500–1680 °C. According to Equation (1), the critical nucleation radius of Al_2O_3 was in the range of 6.79–10.08 nm.

The change of oxide particle size with interface concentration is described as [29]:

$$\frac{dr}{dt} = \frac{M_s}{100M_m r} \frac{\rho_m}{\rho_s} D_L (C_L - C_e) \quad (2)$$

where r is the diameter of the crystal nucleus; D_L is the solute diffusion coefficient in liquid metal; ρ_s is the density of oxide; ρ_m is the density of alloy element; M_s is the molecular weight of oxide; M_m is the molecular weight of alloy element; C_L is the solute concentration in the front of the interface; C_e is the equilibrium solute concentration of the crystal nucleus. The growth driving force of the nano oxide particle was the solute segregation of the solute atom in the front of the oxide interface and the equilibrium concentration of the oxide ($C_L(t) - C_e(t)$), and its growth speed was influenced by the size of the oxide and the solute micro area concentration fluctuations in the front of the interface between oxide and melt. As Figure 9 showed, the growth speed of nano oxide particle was slower with the increase of its radius; meanwhile, its growth speed was reduced sharply, even reduced to zero with the decrease of the [Al] content in the front of the interface. According to Figure 9 and Equation (2), we can conclude that the growth speed of nano oxide particle was proportional to the difference value ($C_L(t) - C_e(t)$), and under a certain temperature, it was only influenced by the [Al] content in the micro area. The growth speed of nano oxide particles in molten steel could be controlled by adjusting these two parameters.

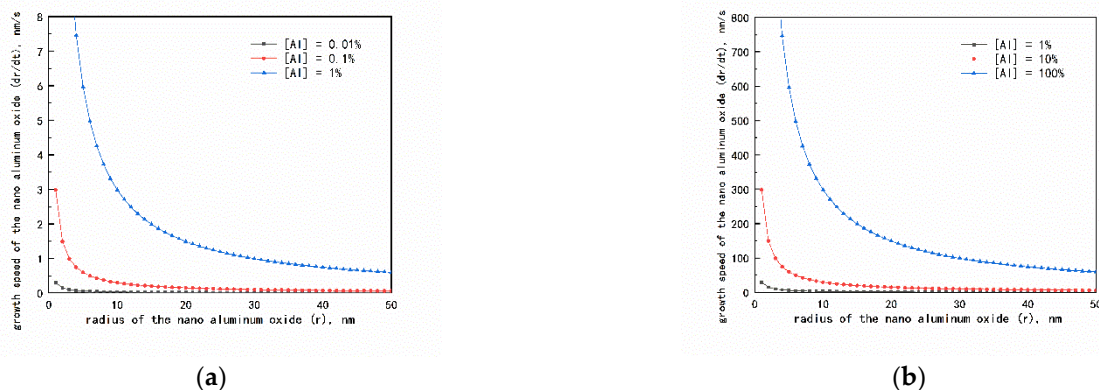


Figure 9. Radius of the nano aluminum oxide particle vs. growth speed under the condition of different [Al] concentration at the temperature of 1873 K; (a) [Al] = 0.01%, 0.1% and 1%; (b) [Al] = 1%, 10% and 100%.

The formation process of oxide inclusions in molten steel could be divided into two stages. In the first stage, when the oxygen concentration in the initial steel was as high as 800–1000 ppm, the growth rate of particles was positively related to the concentration of alloy elements. At this stage, because of the high concentration, the growth rate of oxides was accelerated, and large particle inclusions were formed. It was feasible to remove inclusions floating in the liquid steel. In the second stage, when the oxygen concentration

was low (30 ppm, or even a dozen ppm), the oxide particles formed in the molten steel were smaller (under 10 μm) with the decrease of the oxygen concentration, which cannot be removed in the molten steel. Then, due to the redistribution of solute, the oxygen concentration at the solid-liquid interface increased sharply, and the inclusion particles would further grow up, resulting in a higher final inclusion grade. Therefore, technology of multi-point regional micro-supply in-situ nano particle formation technology was adopted, which schematic diagram was shown in Figure 10. When the oxygen concentration was low (30 ppm), in order to make the inclusions smaller, the twisted Al wire composed of multiple Al wires with small diameter instead of ordinary single Al wire with large diameter were fed in the molten steel. For the same volume of Al, the larger the specific surface area, the smaller the regional concentration of Al in the molten steel. Since the specific surface area of Al wire with small diameter was larger than that of the single Al wire with large diameter, by using multi-point regional micro-supply method the regional concentration of Al generated by contact with the oxygen in the molten steel was lower and the possibility of growing up for oxide particles was smaller. Fine oxide particles would form in the molten steel. At the same concentration, the number of oxide particles increased, which were dispersed in the molten steel. Using the heterogeneous nucleation of fine oxides, the inclusion-forming elements were attached to the fine oxides to refine the inclusions and optimize their shape, as shown in Figure 8, with Al_2O_3 at the core position of the inclusions. The remaining elements were distributed at the core shell, forming a “core-shell” structure.

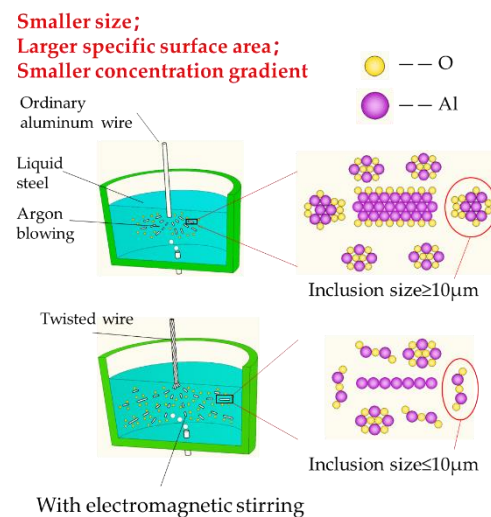


Figure 10. Principle of multi-point regional micro-supply processing of twisted wire by comparing that of ordinary wire.

5. Conclusions

In this work, the new P91 steel fabricated through the method of casting, combined with multi-point regional micro-supply of twisted Al wire during the smelting process, followed by forging has been intensively characterized. The following conclusions can be drawn:

- (1) By comparing with those of traditional P91 steel, four types of inclusions were detected to be refined in the new P91 steel, including: spherical independent Al_2O_3 inclusions, irregular Al_2O_3 - SiO_2 composite inclusions, approximately spherical MgO - Al_2O_3 composite inclusions, and spherical (Ca, Mg, Al) (O) composite inclusions.
- (2) Fine Al_2O_3 can act as heterogeneous nucleation core to form a core-shell type inclusions structure to refine inclusions.
- (3) The smaller the cross-sectional area of the Al wire, the smaller the local concentration generated by contact with the oxygen content in the molten steel, and the smaller the possibility of growing up for Al_2O_3 particles.

- (4) Multi-point regional micro-supply technology is of great significance to refine the inclusions for manufacturing steels.

Author Contributions: Conceptualization: X.C. and Z.W.; methodology: S.L. and Y.W.; software: S.L.; validation: X.C. and Z.W.; formal analysis: Y.W. and W.F.; investigation: W.F. and X.Y.; resources: S.L. and W.F.; data curation: Y.W. and X.Y.; writing—original draft preparation: X.C., S.L. and W.F.; writing—review and editing: X.C. and Z.W.; visualization: W.F.; supervision: X.C., Z.W. and J.Y. All authors have read and agreed to the published version of the manuscript.

Funding: This work was supported by the National Natural Science Foundation of China (52071012, 51971031), the Academic and Technical Leaders of Major Disciplines in Jiangxi Province (20182BCB22020) and the Central Funds Guiding the Local Science and Technology Development-Fundamental Research (YDZX2021005).

Institutional Review Board Statement: Not applicable.

Informed Consent Statement: Not applicable.

Data Availability Statement: The data presented in this study are available upon request from the corresponding author.

Conflicts of Interest: The authors declare no conflict of interest.

References

1. Liu, Y.C.; Xiao, G.Y.; Gao, Z.M. Key Technology Development and Industrialization of P91 Steel Tube for High Pressure Boilers. *Tianjin Sci. Technol.* **2014**, *41*, 9–10.
2. Ennis, P.J. Ferritic and martensitic steels for power plants. In *Structural Alloys for Power Plants*; Amir, S., Susan, J., Eds.; Woodhead Publishing: Sawston, UK, 2014; pp. 188–220.
3. Fan, D.L.; Wang, Z.W.; Ju, G.Y. Microstructure and properties of P91 steel pipeline in abnormal low hardness parts. *Heat Treat. Met.* **2020**, *45*, 1–6.
4. Wu, D.S.; Yang, X.S.; Wu, D.J. Failure Analysis of 12Cr1MoV Alloy Connecting Plate for Ultra-supercritical Unit Boiler. *China Spec. Equip. Saf.* **2019**, *35*, 65–68.
5. Liu, B.; Lu, A.M.; Liu, L.; Liang, Y.; Liu, C.Q. Commercial production practice on steel 12Cr1MoV for boiler tube. *China Metall.* **2015**, *25*, 49–51.
6. Chen, W.; Xu, T.; Liang, J. Analysis on Processing Techniques & Domestication of Four Major Pipes in Power Plants. *Shenhua Sci. Technol.* **2016**, *14*, 12–15.
7. Wang, K.Z.; Hao, Z.Y.; Hu, F.Z.; Chen, S.J.; Huang, Z.Y. Optimization on heat-treatment process of P91 steel for high pressure boiler tubes. *China Metall.* **2018**, *28*, 58–63.
8. Li, X.F.; Zhang, X.F.; Zhang, X.Y.; Wang, S.N. Analysis and Control of Inclusion Defects in 42CrMoA Steel Spindle. *Phys. Exam. Test.* **2020**, *38*, 19–23.
9. Zhang, Y.B.; Pang, Y.S.; Wang, L.H.; Guo, L.; Liu, J.; Chen, S.L. Effect by Nonmetallic Inclusions on Ultrasonic Detection of TP316L Seamless Steel Tube. *Steel Pipe* **2020**, *49*, 43–46.
10. Chan, K.S. A Fatigue Life Model for Predicting Crack Nucleation at Inclusions in Ni-Based Superalloys. *Met. Mater. Trans. A* **2020**, *51*, 1148–1162. [[CrossRef](#)]
11. Du, H.; Karasev, A.; Sundqvist, O.; Jönsson, P. Modification of Non-Metallic Inclusions in Stainless Steel by Addition of CaSi. *Metals* **2019**, *9*, 74. [[CrossRef](#)]
12. Zhang, C.F. Non-metallic inclusions in steel and their influence on properties. *Metall. Mater.* **2020**, *40*, 34–35.
13. Hanif, W.Y.W.; Risby, M.S.; Noor, M.M. Influence of Carbon Nanotube Inclusion on the Fracture Toughness and Ballistic Resistance of Twaron/Epoxy Composite Panels. *Procedia Eng.* **2015**, *114*, 118–123. [[CrossRef](#)]
14. Zhang, Y.; Wu, J.F.; Miao, L.D. Research and Analysis of Reducing Non-metallic Inclusions in P91 Steel Pipe. *Baosteel Technol.* **2008**, 35–40.
15. Simachev, A.S.; Oskolkova, T.N.; Temlyantsev, M.V. Influence of nonmetallic inclusions in rail steel on the high-temperature plasticity. *Steel Transl.* **2016**, *46*, 112–114. [[CrossRef](#)]
16. Murakami, Y.; Kawakami, K.; Duckworth, W.E. Quantitative evaluation of effects of shape and size of artificially introduced alumina particles on the fatigue strength of 1.5NiCrMo (En24) steel. *Int. J. Fatigue* **1991**, *13*, 163–170. [[CrossRef](#)]
17. Sun, C.Q.; Lei, Z.Q.; Xie, J.J.; Hong, Y.S. Effects of inclusion size and stress ratio on fatigue strength for high-strength steels with fish-eye mode failure. *Int. J. Fatigue* **2013**, *48*, 19–27. [[CrossRef](#)]
18. Zhang, K.; Liu, X.B.; Zhu, L. Characterisation of microstructure evolution during creep of P91 steel using the electron backscatter diffraction technique. *Mater. High Temp.* **2021**, *38*, 158–165. [[CrossRef](#)]
19. Sakthivel, T.; Sasikala, G.; Syamala Rao, P.; Parameswaran, P.; Laha, K. Creep deformation and rupture behaviour of boron-added P91 Steel. *Mater. Sci. Technol.* **2021**, *37*, 478–494. [[CrossRef](#)]

20. Kim, W.G.; Lee, H.Y.; Hong, H.U. Evaluation of tension and creep rupture behaviors of long-term exposed P91 steel in a supercritical plant. *Eng. Fail. Anal.* **2020**, *116*, 104736. [[CrossRef](#)]
21. Mo, G.Y.; Yan, B.; You, G. Effect of Non-metallic Inclusions on Lamination Defect in P91 Steel Tubes. *Phys. Test. Chem. Anal. Part A Phys. Test.* **2015**, *51*, 267–269.
22. Liu, J.H.; Zhang, J.; Li, K.W. Current state and prospect of technologies for removing inclusion by bubbles. *Steelmaking* **2017**, *33*, 1–9.
23. Liu, Y.B.; Yang, J. Progress on flow field control technology of tundish. *Contin. Cast.* **2021**, 12–33.
24. Hu, Y.P.; Xu, Y.D.; Shi, B.F.; Han, F.; Tu, M.J. Research on Purified Smelting Process of P91 Heat Resistance Steel. *Heavy Cast. Forg.* **2017**, 30–33.
25. Stefanescu, D.M. *Science and Engineering of Casting Solidification*; Springer: Cham, Switzerland, 2008.
26. Schneider, S.J.; McDaniel, C.L. Effect of Environment Upon the Melting Point of Al_2O_3 . *J. Res. Natl. Bur. Stand. A Phys. Chem.* **1967**, *71*, 317–333. [[CrossRef](#)]
27. Sun, J.Z.; Stirner, T.; Matthews, A. Structure and surface energy of low-index surfaces of stoichiometric $\alpha\text{-Al}_2\text{O}_3$ and $\alpha\text{-Cr}_2\text{O}_3$. *Surf. Coat. Technol.* **2006**, *201*, 4205–4208. [[CrossRef](#)]
28. Dean, J.A. *Lange's Handbook of Chemistry*, 12th ed.; McGraw-Hill: New York, NY, USA, 1979; p. 32.
29. Goto, H.; Miyazawa, K.I.; Yamaguchi, K.I.; Ogibayashi, S.; Tanaka, K. Effect of Cooling Rate on Oxide Precipitation during Solidification of Low Carbon Steels. *ISIJ Int.* **1994**, *34*, 414–419. [[CrossRef](#)]